ACS OMEGA

http://pubs.acs.org/journal/acsodf

Article

Controllable Crystal Growth and Improved Photocatalytic Activity of Porous Bi_2O_3–Bi_2S_3 Composite Sheets

Yuan-Chang Liang,* Yu-Hsun Chou, Bo-Yue Chen, and Wei-Yang Sun

Cite This: *ACS Omega* 2023, 8, 26055−26064

Read Online

ACCESS | Metrics & More | Article Recommendations | Supporting Information

ABSTRACT: Porous Bi_2O_3–Bi_2S_3 composite sheets were constructed through a combinational methodology of chemical bath deposition and hydrothermal reaction. The Na_2S precursor concentration in the hydrothermal solution was varied to understand the correlation between the vulcanization degree and structure evolution of the porous Bi_2O_3–Bi_2S_3 composite sheets. The control of the etching rate of the Bi_2O_3 sheet template and the regrowth rate of Bi_2S_3 crystallites via suitable sulfide precursor concentration during the hydrothermal reaction utilizes the formation of porous Bi_2O_3–Bi_2S_3 sheets. Due to the presence of Bi_2S_3 crystallites and porous structure in the Bi_2O_3–Bi_2S_3 composites, the improved visible-light absorption ability and separation efficiency of photogenerated charge carriers are achieved. Furthermore, the as-synthesized Bi_2O_3–Bi_2S_3 composite sheets obtained from vulcanization with a 0.01M Na_2S precursor display highly enhanced photocatalytic degradation toward methyl orange (MO) dyes compared with the pristine Bi_2O_3 and Bi_2S_3. The porous Bi_2O_3–Bi_2S_3 sheet system shows high surface active sites, fast transfer, high-efficiency separation of photoinduced charge carriers, and enhanced redox capacity concerning their constituent counterparts. This study affords a promising approach to constructing Bi_2O_3-based Z-scheme composites with a suitable microstructure and Bi_2O_3/Bi_2S_3 phase ratio for photoactive device applications.

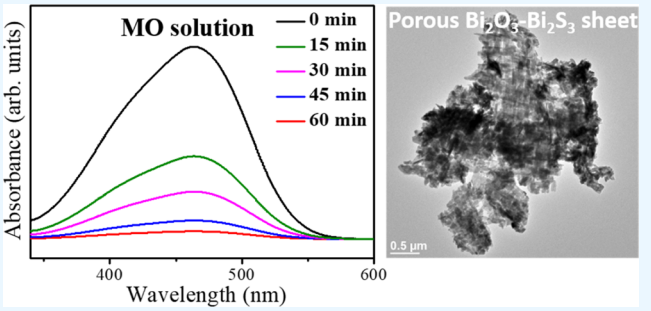

INTRODUCTION

Satisfactorily, semiconductor-based photocatalysis is an eco-friendly and efficient technology to tackle the problem, which utilizes renewable solar energy to remove the organic dyes without any secondary pollutants. Bi_2S_3 and Bi_2O_3 are two important semiconductors extensively investigated for scientific applications. Bi_2S_3 is a narrow bandgap semiconductor with great promise in numerous photosensitive device applications.[1−5] Due to unique shape- and size-dependent physical and chemical properties, Bi_2S_3 crystals with a large growth scale and different morphologies have been synthesized through various chemical routes.[1−3] Moreover, Bi_2S_3 absorbs visible light and can be used as a visible-light photocatalyst.[6,7] However, due to the facile recombination of photogenerated electrons and holes, the photocatalytic performance of Bi_2S_3 crystals is still highly desirable for substantial improvement. In addition, Bi_2O_3 has various phases and is also a visible light-sensitive semiconductor.[8−10] It has been widely used in various photosensitive device applications due to its stable chemical nature, various morphologies, and diverse synthesis routes.[11−14]

Although Bi_2S_3 and Bi_2O_3 semiconductors have superior light harvesting abilities because of their narrow bandgap energies, their photoinduced charge separation efficiency under irradiation still needs marked improvement to make them suitable for photosensitive device applications with high performance. One promising strategy to improve the photoinduced charge separation efficiency in a single photosensitizer component is to couple it with another semiconductor to construct a suitable band alignment and enhance photoactive performance. It has been shown that Bi_2S_3 coupled with TiO_2 or $Bi_2O_2CO_3$ to form Bi_2S_3–TiO_2 and Bi_2S_3–$Bi_2O_2CO_3$ heterogeneous systems demonstrates enhanced photoactive performance for photosensitive device applications.[15,16] Furthermore, Bi_2O_3-based heterogeneous systems such as Bi_2O_3–BiOCl, $CuBi_2O_4$–Bi_2O_3, and TiO_2–Bi_2O_3 all demonstrate improved photoactive performance compared with their single constituent counterparts.[11,12,17] Based on the above discussion, it might be interesting to integrate Bi_2S_3 with Bi_2O_3 to form a heterogeneous system and investigate the photoactive performance of this hybrid system. A well-defined Bi_2O_3–Bi_2S_3 composite has been synthesized using an ultrasonic-assisted synthetic method on a conductive substrate, and the resulting Bi_2O_3–Bi_2S_3 composite shows highly

Received: March 30, 2023
Accepted: July 4, 2023
Published: July 13, 2023

enhanced photoelectrochemical activity.[18] Branched Bi_2O_3−Bi_2S_3 composites synthesized by a simple hydrothermal method without toxic substances demonstrate high photocatalytic activity under visible-light illumination.[19] These examples present the feasibility of constructing a Bi_2S_3−Bi_2O_3 heterogeneous system for a photoactive device with improved efficiency.

Notably, looking into the synthesis routes developed for generating Bi_2S_3-based composites, shortcomings such as the use of harmful solvents and additives and the need for complex synthesis processes are generally involved.[16] It has been shown that Bi_2O_3 is a material with a high tendency for sulfurization.[20] This study will develop the vulcanization process to form Bi_2O_3−Bi_2S_3 sheet composites to avoid the generally involved shortcoming of using harmful solvents and additives during material synthesis. The hydrothermally induced vulcanization reaction on a chemical bath deposition (CBD)-derived Bi_2O_3 sheet template is adopted to prepare Bi_2O_3−Bi_2S_3 sheet composites. This synthesis methodology of Bi_2O_3−Bi_2S_3 sheet composites is environment-friendly because hydrothermally induced vulcanization uses no toxic solvents or surfactants. Meanwhile, the initially porous Bi_2O_3 sheet template for growing Bi_2O_3−Bi_2S_3 sheet composites has the advantage of large surface active sites and improves photoactive efficiency.[8] The photosensitive property of the as-prepared Bi_2O_3−Bi_2S_3 composites was studied, and they displayed enhanced photosensitivity compared with the pristine Bi_2O_3 and Bi_2S_3. This excellent photoactive performance benefits from the increased light absorption, matched energy band alignment of Bi_2O_3/Bi_2S_3, and improved separation and transfer efficiency of photogenerated electron−hole pairs. The exact correlation between the vulcanization process-dependent microstructures and the photoactive performance of the Bi_2S_3−Bi_2O_3 sheet composites is proposed in this study.

EXPERIMENTS

The Bi_2O_3−Bi_2S_3 composites were prepared by a two-step synthesis method. The first step is to prepare a porous Bi_2O_3 sheet template using chemical bath deposition (CBD). According to previous work, the porous Bi_2O_3 sheet films were grown on F-doped tin oxide (FTO) glasses by the CBD method.[8] The 0.1 M bismuth nitrate was dissolved in deionized water to make a 50 mL stock solution. Furthermore, 3 mL of triethanolamine (TEA) and 0.2 M NaOH were added to the solution above to form a highly alkaline solution with a pH = 10. The CBD reaction was conducted at 65 °C for 2 h. After cooling to room temperature naturally, the FTO substrate with a layer of whitish film was washed with deionized water several times. Finally, the substrate was annealed at 300 °C for 1 h in air ambient to obtain porous Bi_2O_3 sheet films. Furthermore, the Bi_2O_3−Bi_2S_3 composites were prepared via a hydrothermal route. First, 0.01, 0.1, and 1 M Na_2S precursor solutions with 12.5 mL were transferred into Teflon-lined stainless-steel autoclaves. The as-prepared porous Bi_2O_3 sheet films were placed into the autoclave with the film side facing down. The hydrothermal reaction was conducted at 160 °C for 3 h. The final products were collected and washed with deionized water several times and dried in air at 60 °C. The samples prepared at 0.01, 0.1, and 1 M Na_2S precursor solutions are coded S1, S2, and S3 in this study.

The crystal structure of pristine Bi_2O_3, S1, S2, and S3 was determined by X-ray diffraction (XRD; Bruker D2 PHASER) with monochromatic Cu-Kα radiation in the two theta ranges of 20−60°. Field emission scanning electron microscopy (SEM; S-4800 Hitachi) investigates the surface morphology of prepared samples. High-resolution transmission electron microscopy (HRTEM; Philips Tecnai F20 G2) was operated at 200 kV to investigate the microstructure of samples. X-ray photoelectron spectroscopy (XPS ULVAC-PHI, PHI 5000 VersaProbe) recorded the elemental binding states of samples with argon ion sputtering to remove surface contamination. The etching depth herein is approximately 20 nm. The absorption spectra of samples were obtained using a UV−vis spectrophotometer (JASCO V750). Photoelectrochemical (PEC) and electrochemical impedance spectroscopy (EIS) properties of samples were investigated using the potentiostat (SP150, BioLogic). Herein, the as-prepared sample was used as the working electrode with an active area of 1 cm^2. Meanwhile, a saturated Ag/AgCl (in saturated KCl) electrode and a Pt wire served as the reference and counter electrodes, respectively. An aqueous solution of 0.5 M Na_2SO_4 was used as the electrolyte. A 100 W Xe lamp was used as the illumination source, and the pure visible light was obtained using a 420 nm cutoff filter. The photodegradation experiment used the 10 mL methyl orange (MO) solution (5×10^{-5} M) as the target dye solution. The dark absorption−desorption equilibrium was conducted for 60 min. A 100 W Xe lamp with a 420 nm UV light cutoff filter was used as the visible light source. After the light irradiation, the MO solution with different photocatalytic reaction durations (0, 15, 30, 45, and 60 min) was taken out by the syringe for analyzing the residual concentration with a UV−vis spectrophotometer.

RESULTS AND DISCUSSION

Figure 1a shows that the vertically aligned and uniform sheet-like Bi_2O_3 array was grown on the FTO substrate. The diameter of the sheets is approximately 2.5−3.5 μm. Moreover, great tiny pores were found in the Bi_2O_3 sheets. Figure 1b displays the SEM image of S1. After 0.01 M vulcanization of the Bi_2O_3 sheet template, S1 still exhibited a sheet-like morphology similar to the pristine Bi_2O_3 but with a substantially decreased size. Notably, the bamboo-like crystallites cross-linked with each other to form the sheet morphology, and pores existed between them. When the concentration of vulcanization was increased to 0.1 M, the size of the sheet structure of S2 increased, as revealed in Figure 1c. Notably, numerous tiny pores are exhibited on the S2 surface. The structure became looser in comparison with that of S1. Figure 1d presents the highest sulfurization concentration (1 M), making S3 display a significant sheet size change compared to S1 and S2. The sheet size of S3 was markedly large. Furthermore, no pores were observed on the S3 surface, which was relatively smooth. It has been shown that pristine Bi_2O_3 sheets will be etched, and regrowth of Bi_2S_3 occurs under enough sodium sulfide vulcanization reaction.[19] Less S^{2-} ions are expected at a low reaction concentration of 0.01 M; therefore, small and solid Bi_2S_3 crystallites will be formed after etching partial parent Bi_2O_3 sheets. The as-formed Bi_2S_3 oval crystallites are connected to form S1. Sulfur ions replaced the surface oxygen ions of the Bi_2O_3 template because of ion exchange during the vulcanization process. The etching rate of the Bi_2O_3 sheets and the regrowth rate of Bi_2S_3 crystallites competed during the hydrothermal reaction.[20] As the Na_2S concentration increased, both the etching rate of the Bi_2O_3 and the regrowth rate of the Bi_2S_3 increased. The Bi_2S_3 crystallites will produce more and form a larger sheet structure of S2

https://doi.org/10.1021/acsomega.3c02153
ACS Omega 2023, 8, 26055−26064

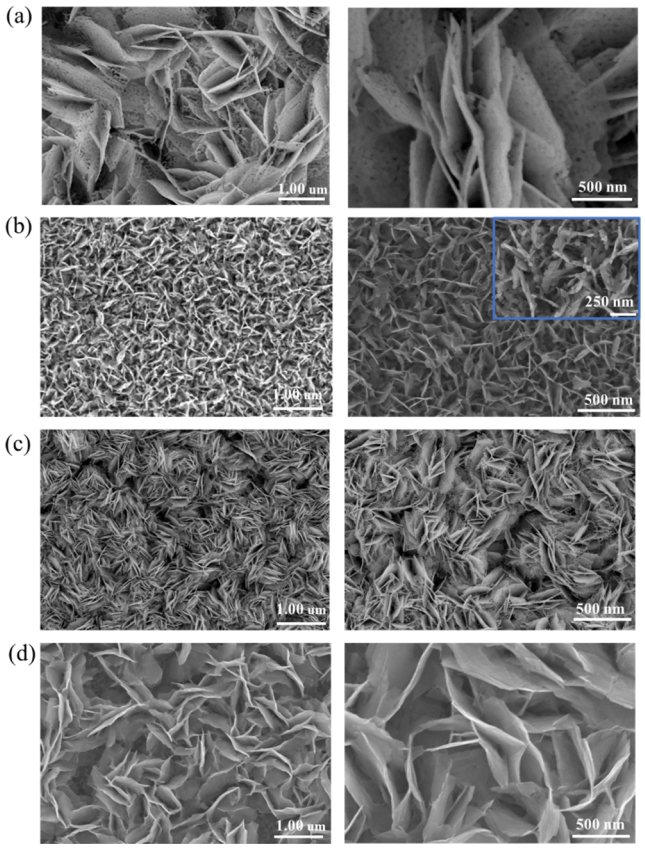

Figure 1. SEM micrographs of various sheets: (a) Bi_2O_3. (b) S1. (c) S2. (d) S3.

under the reaction condition. Finally, the parent Bi_2O_3 sheets will be fully etched at 1 M vulcanization conditions and wholly converted into Bi_2S_3 crystals. The sufficient Bi_2S_3 crystallites are densely contacted to form the solid, smooth, and sizeable Bi_2S_3 sheet structure of S3.

Figure 2a presents the XRD pattern of the Bi_2O_3 sheet template. Except for the diffraction peaks of the FTO substrate, the characteristic peaks of tetragonal-structured β-Bi_2O_3 are indexed (JCPDS 27-0050). The XRD result shows that CBD successfully synthesized the high-purity Bi_2O_3 phase, and the crystal growth plane of Bi_2O_3 was mainly (201) orientation. The XRD patterns of S1 and S2 are shown in Figure 2b,c, respectively. The sharp Bragg reflection peaks in the XRD patterns indicate that the as-synthesized products comprise the orthorhombic Bi_2S_3 phase (JCPDS 17-0320) and the tetragonal Bi_2O_3 phase. The XRD patterns reveal that the Bi_2O_3–Bi_2S_3 composite was successfully synthesized through the vulcanization method. Comparatively, in Figure 2b,c, it is found that when the Na_2S concentration was increased, the Bragg reflection intensity of the Bi_2O_3 phase markedly decreased, and the Bragg reflection intensity of the Bi_2S_3 phase increased. This reveals an increased Bi_2S_3 phase content in the Bi_2O_3–Bi_2S_3 composite with an increased Na_2S concentration during vulcanization. By contrast, after the vulcanization concentration is increased to 1 M, the XRD pattern of S3 in Figure 2d does not show the characteristic peak of the Bi_2O_3 phase, indicating the complete consumption of the Bi_2O_3 sheet template to form Bi_2S_3 crystals under this vulcanization condition.

Figure 3a,b shows morphological images of S1. The S1 sheets are formed by numerous oval crystallites linked to form a sheet structure, and abundant nanopores exist in the sheet structure. The diameter of the sheet is approximately 0.6–0.8 μm. The HRTEM images in Figure 3c,d show that the ordered lattice fringes with spacings of 0.25 nm and 0.32 nm are attributed to the interplanar distances of Bi_2S_3 (240) and Bi_2O_3 (201), respectively. The HRTEM images show powerful proof of the composite structure of Bi_2O_3 and Bi_2S_3 in S1. Figure 3e displays the selected area electron diffraction (SAED) of the randomly selected area of the sheet. The pattern exhibited sharp and bright spots arranged in several centric rings. The SAED pattern feature indicates the polycrystalline nature of the synthesized S1. According to the SAED pattern, the (201), (220), and (222) crystallographic planes were determined to correspond to the tetragonal Bi_2O_3 phase. The (220), (101), (130), (211), (240), (141), and (421) crystallographic planes were determined to correspond to the orthorhombic Bi_2S_3 phase. In addition, the line-scan energy dispersive X-ray spectroscopy (EDS) spectra profiles (Figure 3f) of the S1 sheet display that the Bi, O, and S elements are well distributed in the product. The O is concentrated in the center area, Bi is distributed equally on the whole sheet, and S is mainly distributed in the peripheral areas. The elemental distribution results confirm that both the etching and regrowth processes started from the periphery of the parent Bi_2O_3 and reveal that the Bi_2O_3–Bi_2S_3 composite was formed because of an insufficient vulcanization process that results in residual Bi_2O_3 crystals in S1.

The representative low-magnification TEM images in Figure S1a,b also confirm that S2 has a sheet-like structure and great tiny pores on the sheet. The diameter of the sheet can reach approximately 1.3–1.6 μm. The TEM images herein are consistent with the SEM inspections. Figure S1c,d shows the local HRTEM micrographs of positions c and d marked in Figure S1b, respectively. Two different lattice fringes with spacings of approximately 0.25 and 0.32 nm could be resolved in Figure S1c,d, which agree well with the interplanar distances of Bi_2S_3 (240) and Bi_2O_3 (201), respectively. In addition, the heterogeneous Bi_2O_3–Bi_2S_3 sheet feature can be recognized by the grayscale contrast in the HRTEM images, in which Bi_2O_3 shows darker contrast while the Bi_2S_3 shows brighter contrast. Figure S1e shows the SAED pattern taken from Figure S1a; the pattern feature reveals the polycrystalline nature of S2 and the coexistence of the Bi_2O_3 and Bi_2S_3 phases. The EDS line scan profiles in Figure S1f display that Bi is evenly distributed on the entire sheet, while S is mainly distributed in the peripheral area. Notably, the O element is concentrated in the small central area. This result confirms the formation of a Bi_2O_3–Bi_2S_3 heterostructure of S2.

Figure 4a presents a morphological image of S3. Compared with S1 and S2, S3 has a denser and solid sheet structure. The diameter of the S3 sheet is approximately 2.0–2.4 μm and is markedly more prominent than S1 and S2. Figure 4b,c shows HRTEM images of different regions in Figure 4a. The lattice fringes with multiple orientations are observed in the HR images, which reveal the polycrystalline feature of the sheet structure. The lattice fringe distances of 0.25 nm and 0.35 nm corresponded to the interplanar spacings of Bi_2S_3 (240) and (130), respectively. Figure 4d shows the SAED pattern of the sheet structure in Figure 4a, and the pattern exhibits several diffraction rings consisting of sharp and bright spots that originated from various Bi_2S_3 crystallographic planes. Fur-

https://doi.org/10.1021/acsomega.3c02153
ACS Omega 2023, 8, 26055–26064

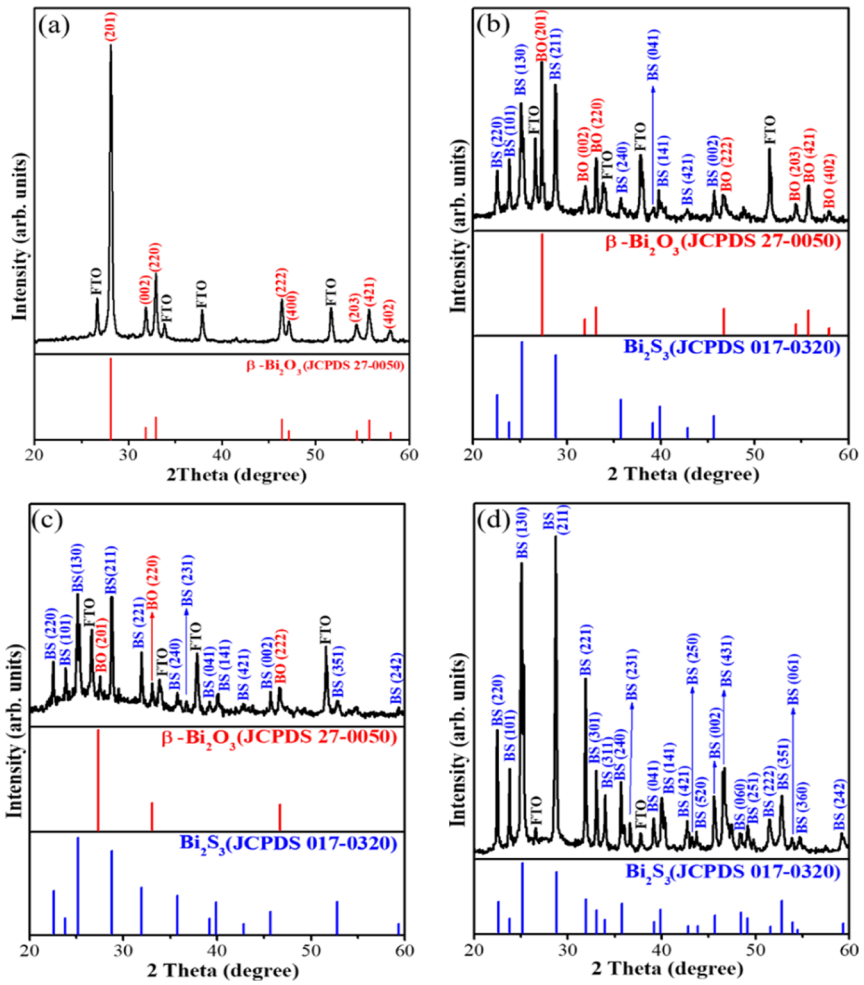

Figure 2. XRD patterns: (a) Bi_2O_3. (b) S1. (c) S2. (d)S3. BO and BS denote Bi_2O_3 and Bi_2S_3, respectively.

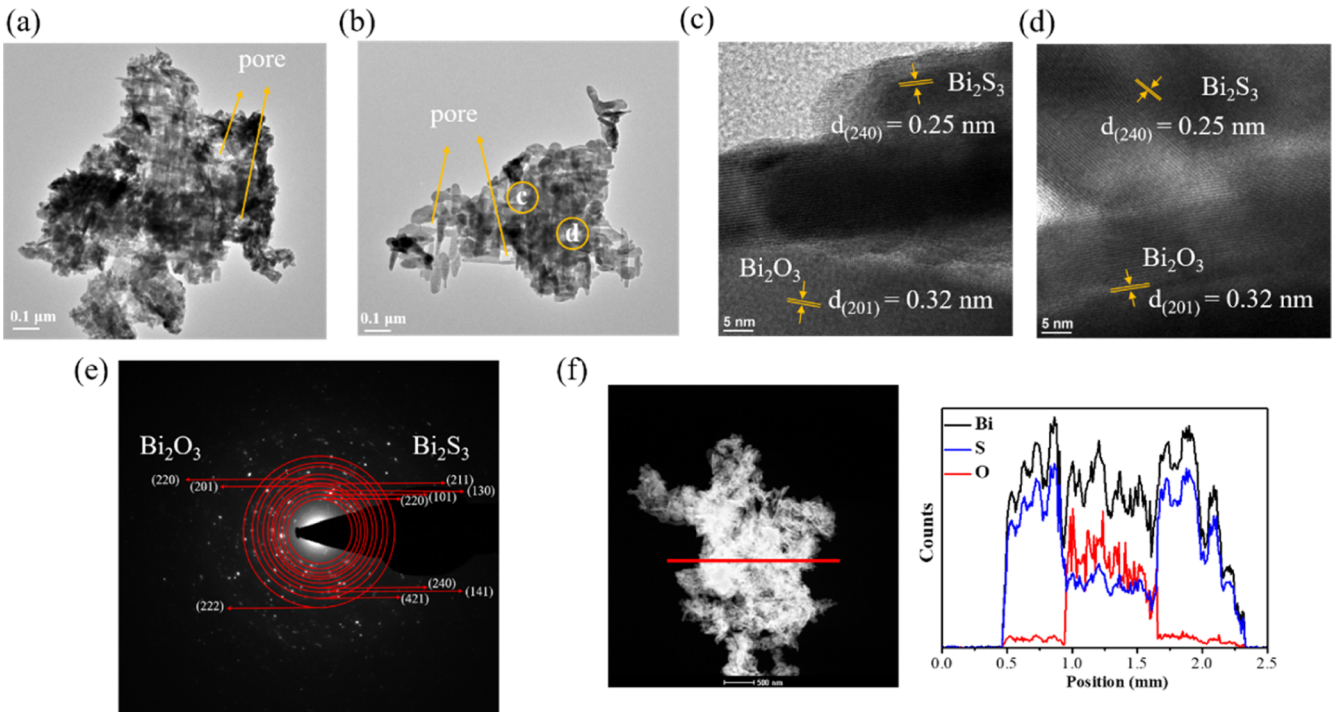

Figure 3. TEM analysis of S1: (a,b) low-magnification images. (c,d) HRTEM images. (e) SAED pattern. (f) EDS line-scan profiles of the sample.

https://doi.org/10.1021/acsomega.3c02153
ACS Omega 2023, 8, 26055−26064

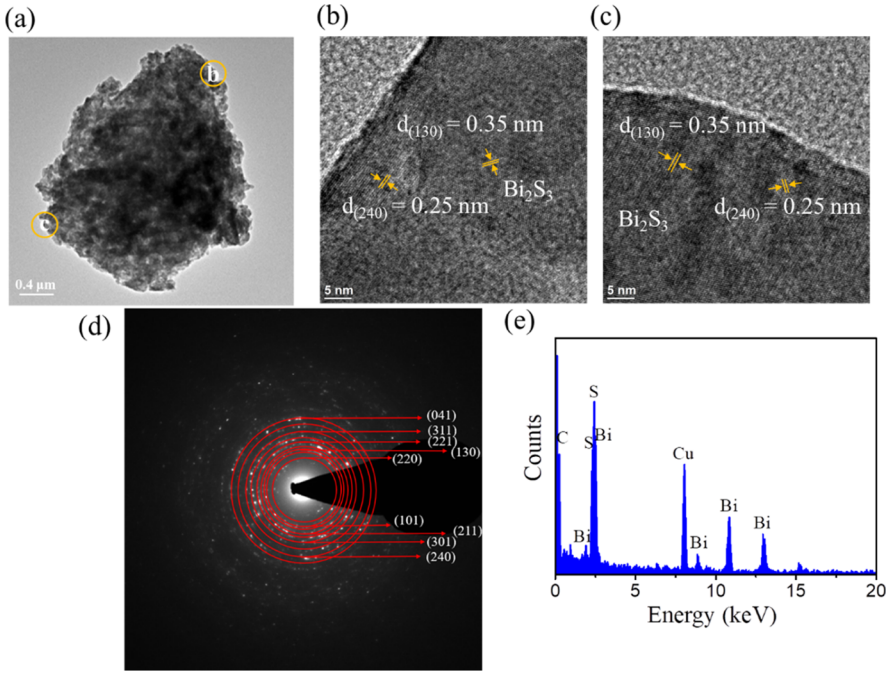

Figure 4. TEM analysis of S3: (a) low-magnification image. (b,c) HRTEM images. (d) SAED pattern. (e) EDS spectrum of the sample.

thermore, the chemical composition of S3 was characterized by the EDS spectrum (Figure 4e). Figure 4e shows that only Bi and S are the primary constituent elements of S3, and the C and Cu signals come from the TEM grid. Further quantitative analysis demonstrates that the molar ratio of Bi and S is close to 2:3, in good agreement with the stoichiometric composition of Bi_2S_3. The TEM analysis reveals that S3 is in a pure Bi_2S_3 phase.

When the Bi_2O_3 sheet template was vulcanized with a 0.01 M Na_2S precursor, the S 2p signal appeared between the Bi $4f_{5/2}$ and $Bi4f_{7/2}$ peaks, as revealed in Figure S2a. The appearance of the S2p peak presents the formation of the sulfide phase through vulcanizing the Bi_2O_3 layer in the product, in which the S2p peak feature is not shown between the Bi 4f core-level peaks of the Bi_2O_3 sheet template.[8] The binding energies of Bi 4f core-level peaks for S1 present the characteristic binding state of Bi^{3+} in the Bi_2S_3.[21] Furthermore, the symmetric Bi 4f peaks reveal no metallic Bi appearing in the product after the vulcanization process. Figure S2b presents the O 1s spectrum of S1, and the appearance of the O 1s peak demonstrates that the product contains residual Bi_2O_3 phase, and the binding energies of the deconvoluted subpeaks in the O 1s spectrum show the bindings of lattice oxygen and adsorption oxygen species in the product.[8] Figure S2c displays the Bi4f XPS spectrum of S3; a more intense S 2p signal was observed than S1. Furthermore, no O 1s signal was detected, supporting the formation of pure Bi_2S_3 crystals, as observed in previous structural analysis results.

The optical absorption spectra of Bi_2O_3, S1, S2, and S3 are shown in Figure 5. The absorption edge of the pristine Bi_2O_3 sheet template is located at around 542 nm, which is consistent with the inherent band gap absorption of tetragonal β-Bi_2O_3.[22] Furthermore, the light absorption range was appreciably widened and red-shifted for S1, S2, and S3. From the aforementioned structural analysis, S3 is a pure Bi_2S_3 phase, and its bandgap energy is evaluated to be approximately 1.37 eV in Figure S3 according to the plot of the modified

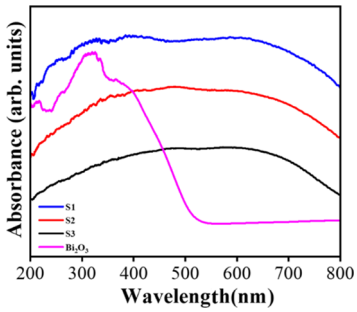

Figure 5. Absorbance spectra of various samples.

Kubelka–Munk function versus the photon energy.[8] This bandgap energy is close to the previously reported value of Bi_2S_3 nanorods.[23] The light absorption result demonstrates that when the heterogeneous Bi_2O_3–Bi_2S_3 was formed in S1 and S2, a substantial red-shift of the absorption edge occurred concerning the pristine Bi_2O_3. The Bi_2O_3–Bi_2S_3 composites could utilize more light and produce photogenerated charge carriers than the initial Bi_2O_3 sheet template.

Figure 6a shows the transient photocurrent response of various samples under chopped illumination. Upon illumination, the photocurrent density of the samples increases rapidly, and the photocurrent density decreases instantaneously with the removal of illumination. The photocurrent density of each sample remains stable after cycling tests. The higher the photocurrent density is, the more efficient the separation efficiency of photoinduced charge carriers is, and then S1 is supposed to exhibit more efficient photoactive performance. When the light is turned on, Bi_2O_3, S1, S2, and S3 all show different degrees of spike-like transient response associated with recombining the photoinduced carriers at the surface states of semiconductors.[24] The order of photocurrent intensity is as follows: S1 > S2 > Bi_2O_3 > S3. S1 shows the highest photocurrent density (0.14 mA/cm^2) among all the samples. Furthermore, the Bi_2O_3–Bi_2S_3 composites (S1 and

https://doi.org/10.1021/acsomega.3c02153
ACS Omega 2023, 8, 26055−26064

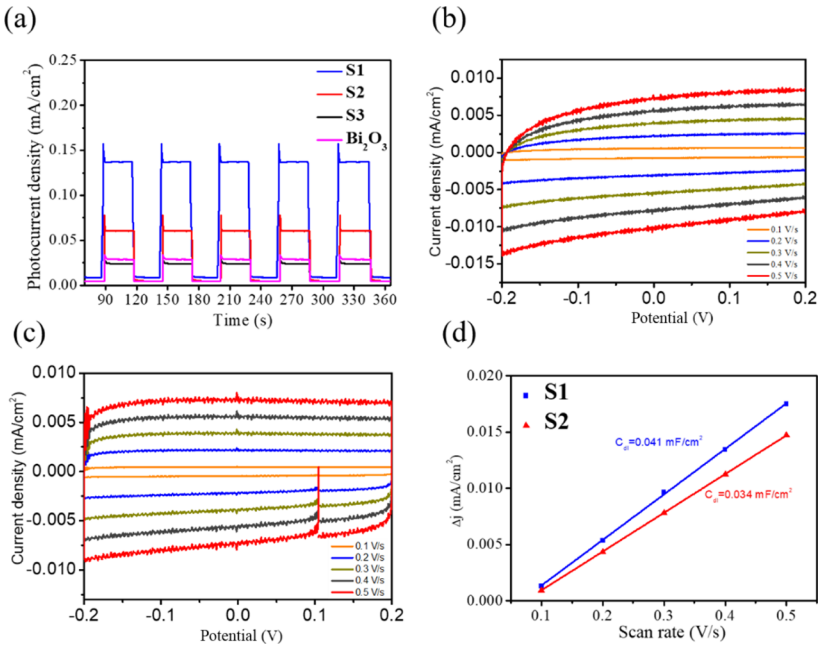

Figure 6. (a) Transient photocurrent density versus time curves of various samples under chopped irradiation at 1.5 V. CVs measured in the non-faradaic region of −0.20 to 0.20 V vs NHE with different scan rates: (b) S1. (c) S2. (d) Scan rate-dependent current density plots of S1 and S2.

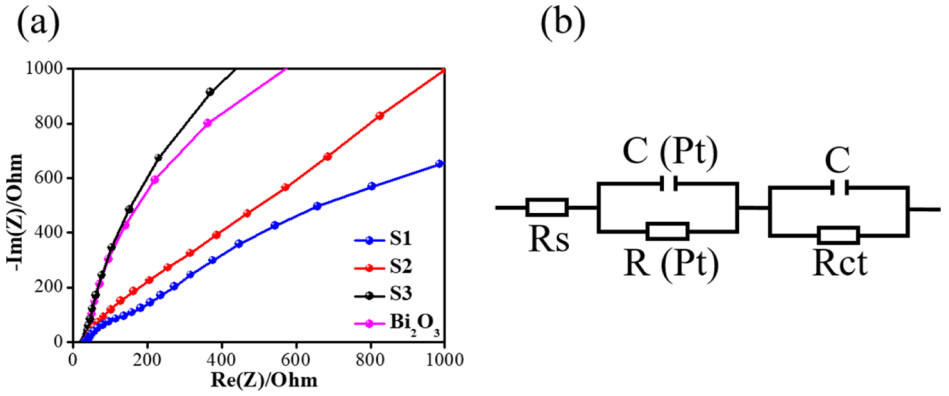

Figure 7. (a) Nyquist plots of various samples under light irradiation. (b) Possible equivalent circuit used for R_{ct} evaluation of composite samples.

S2) show a higher photoresponse than the pristine Bi_2O_3 and Bi_2S_3, which is powerful evidence to verify the excellent photoresponse in the heterogeneous structure. S1 has a higher photoresponse performance than that of S2 herein can be attributed to several reasons. First, the photogenerated carriers are effectively separated due to Bi_2O_3 being maintained as the main body in S1. Although Bi_2S_3(S3) shows a wider absorption than Bi_2O_3, its photocurrent intensity is lower than that of Bi_2O_3. This might be due to the narrower band gap of Bi_2S_3(S3), which makes the photogenerated electrons and holes easy to recombine.[19] Second, S1 and S2 are in different morphologies. The markedly smaller sheet size and abundant pores in S1 could lead it to exhibit more surface active sites than S2, which can be characterized by electrochemically active surface area (ECSA). The cyclic voltammetry curves of S1 and S2 at various scanning rates (0.1, 0.2, 0.3, 0.4, and 0.5 V/s) are recorded in Figure 6b,c, respectively. The electric double-layer capacitance value (C_{dl}) has been used to measure the ECSA, as it reflects the intrinsic activity of the catalyst. There is a linear relationship between the ECSA size and C_{dl}.[25] The C_{dl} values from cyclic voltammetry curves at non-faradaic potential regions (−0.2 to 0.2 V) can be extracted by plotting the $\Delta j = j_a - j_c$ at the middle potential against the scan rate, where j_a is the anode current and j_c is the cathode current. $C_{dl} = \Delta j/2\nu$, and ν is the scan rate in mV s^{-1}. The extracted slopes of Δj vs scan rate plot allow a comparison of the ECSA between S1 and S2.[26] In Figure 6d, the C_{dl} of S1 is 0.041 mF cm^{-2}, nearly 1.2 times larger than that of S2 (0.034 mF cm^{-2}). The work of open-ended Fe_2O_3@CuO nanotubes with high porosity ensures sufficient electrolyte diffusion, revealing more active sites that could be exposed in the reaction environment.[27] A larger ECSA of S1 than that of S2 was visibly displayed. Such a larger ECSA exposes the sample to more active sites, maintaining the sufficient electrochemical reaction between the S1 and electrolyte ions and thus delivering high photo-/electrocatalytic performance.[28] The positive contribution of ECSA size to the PEC performance in other materials systems supports the observed results in this study.[29]

EIS investigated the samples' carrier transport and recombination dynamics under light illumination. Figure 7a shows the Nyquist plots of various samples. The arc radius size of Nyquist plots is proportional to the charge-transfer

https://doi.org/10.1021/acsomega.3c02153
ACS Omega 2023, 8, 26055−26064

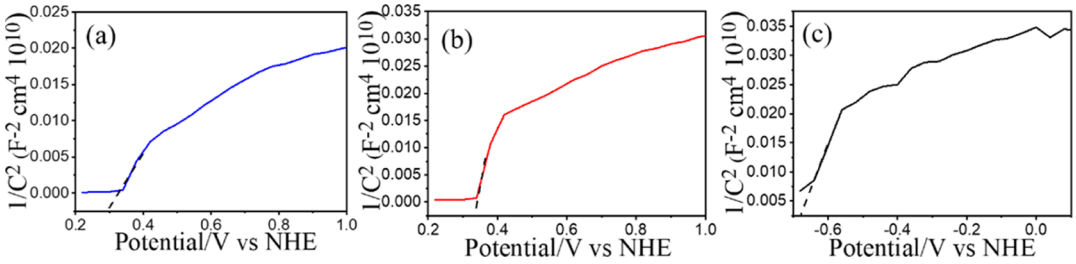

Figure 8. Mott−Schottky plots: (a) S1. (b) S2. (c) S3. The Mott−Schottky plots are obtained in a 0.5 M Na_2SO_4 solution at 1 kHz.

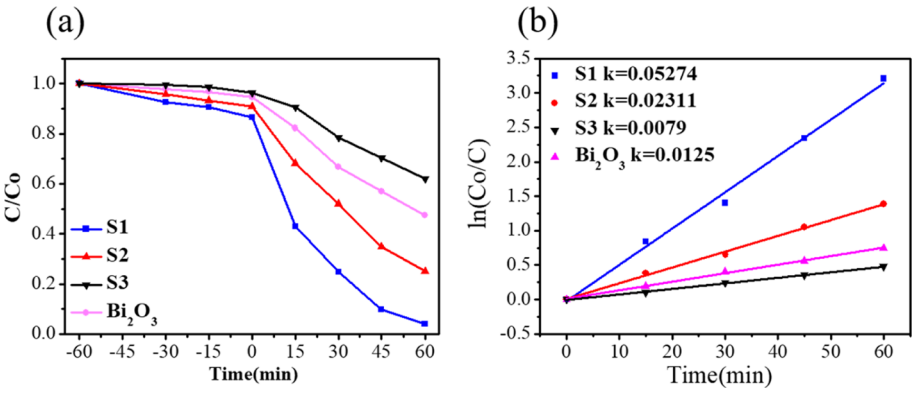

Figure 9. (a) C/C_o vs irradiation time plot. (b) Plot of ln (C_o/C) vs irradiation time for various samples.

resistance of semiconductors.[30] In Figure 7a, the pristine Bi_2O_3 and Bi_2S_3 (S3) have a larger semicircle radius compared to the heterogeneous samples (S1 and S2). Moreover, S1 shows the smallest radius, implying the minimum electron-transfer resistance and the fastest interface electron-transfer rate among various samples. Figure 7b exhibits the possible equivalent circuits for a quantitative analysis of the interfacial charge-transfer ability of the S1 and S2 composites. As the illustrations show, the intercept of the semicircle in the high-frequency region with a real axis symbolizes the solution resistance Rs. It depends on the electrolyte's concentration and conductivity.[31] C is a typical double-layer capacitance for the electrode surface.[32] R_{ct} is the electron-transfer resistance, and it can be estimated through the fitting of arc radii of the Nyquist curves. Moreover, R (Pt) and C (Pt) are the resistance and ordinary double-layer capacitor of the Pt counter electrode, respectively.[33] The R_{ct} values of S1 and S2 are estimated to be approximately 297 and 541 Ω, respectively. For comparison, the R_{ct} values of the pristine Bi_2O_3 (1152 Ω) and S3 (1341 Ω) are also shown herein. The interfacial charge-transfer resistance was markedly reduced in the Bi_2O_3−Bi_2S_3 hybrid system. In conclusion, S1 exhibits fast interfacial charge transfer and practical carrier separation ability, which reduces the interfacial resistance, proving that the Bi_2O_3−Bi_2S_3 heterostructure with a suitable composition phase ratio helps to separate the photoexcited electron−hole pairs.

Figure 8 shows the Mott−Schottky (M−S) plots of S1, S2, and S3. Flat band potentials of all samples were calculated based on the intercept by extrapolating the linear part of the M−S plots to the *x*-axis. From Figure 8a−c, the flat band potential values of S1, S2, and S3 are approximately 0.29, 0.35, and −0.67 V, respectively (V vs NHE). The M−S curve benefits the determination of the position of the conduction band (CB). However, S1 and S2 are heterogeneous structures herein; their heterogeneous band alignment cannot be known directly from the M−S plots. By contrast, S3 is a pure Bi_2S_3 phase; the CB position can be evaluated from the flat band potential in Figure 8c. In general, the flat band potential of n-type semiconductors is about 0.1 V below the CB.[34] Hence, the CB position (E_{CB}) values of Bi_2S_3 herein are estimated to be approximately −0.57 V; this value agrees with the reported value.[35] Considering the aforementioned calculated bandgap energy of S3, the valence band energy (E_{VB}) of Bi_2S_3 is estimated to be approximately 0.80 V, based on $E_g = E_{VB} - E_{CB}$. For S1 and S2, the heterogeneous band alignment can be constructed from understanding the CB and VB positions of the Bi_2O_3 and Bi_2S_3 phases. The CB and VB positions of the Bi_2O_3 phase under similar synthesis conditions have been reported elsewhere.[8] Furthermore, the density of charge carriers among various samples can be compared from the slope of the M-S plot. According to the relationship between $1/C^2$ and the applied potential (V), wherein C is interfacial capacitance.[36] The tangent slope of the M−S plots is inversely proportional to the carrier density size of a semiconductor.[24] According to the estimated slope size, the carrier density size of various vulcanization samples follows S3 < S2 < S1. The result indicates that Bi_2O_3−Bi_2S_3 heterostructures showed higher charge carrier separation efficiencies than their single constituent counterparts; the M−S analysis results herein supported the observations of the PEC above photoresponse results.

The photocatalytic activities of various samples were evaluated by photocatalytic degradation of MO aqueous solution under visible light irradiation (wavelength > 420 nm). The photodegradation efficiency of the MO solution with various photocatalysts is summarized in Figure 9a. The ratio of the residual concentration (C) to the initial concentration (C_o) of the MO solution was used as the photodegradation degree.[37] Notably, the dark balance tests are conducted at the equilibrium state of the adsorption−desorption process for 60 min. The C/C_o decreased 13.5, 9.3, 3.4, and 5.5% for S1, S2, S3, and Bi_2O_3 under dark balance conditions, respectively. S1

https://doi.org/10.1021/acsomega.3c02153
ACS Omega 2023, 8, 26055−26064

has the best surface dye adsorption capacity. This is supported by the SEM observations that S1 has a small sheet size and is more porous than other vulcanization samples, which increases the surface area and surface adsorption. The worst surface dye adsorption capacity of S3 is mainly due to its large and solid sheet morphology engendered a smaller surface area among various samples. The sequential MO dye degradation rates are S3 < Bi_2O_3 < S2 < S1. Nearly complete photodegradation (approximately 95%) of the MO solution was achieved with S1 after 60 min of irradiation. S2, S3, and Bi_2O_3 photodegraded 75, 38, and 52% MO dyes after 60 min of irradiation, respectively. Compared to the single component S3 and Bi_2O_3, the Bi_2O_3−Bi_2S_3 composites (S1 and S2) exhibit enhanced photocatalytic properties. The photocatalytic activities of S1, S2, S3, and Bi_2O_3 are further compared with the pseudo-first-order rate constant k herein according to the pseudo-first-order model.[38] The corresponding fitted kinetics curves of various samples are shown in Figure 9b. The k of S1, S2, S3, and Bi_2O_3 is 0.0527, 0.0231, 0.0079, and 0.0125 min^{-1}, respectively. S1 exhibits the highest reaction rate constant k among various samples. The porous structure, high charge separation efficiency, and low interfacial charge-transfer resistance account for the superior photocatalytic activity of S1 in this study.

Trapping experiments of reactive species during the photocatalytic process of S1 toward MO solution were conducted to understand the possible photodegradation mechanism. Three different quenchers, benzoquinone (BQ; a $^{\bullet}O_2^-$ radical scavenger), isopropyl alcohol (IPA; a $^{\bullet}OH$ radical scavenger), and ammonium oxalate (AO; an h^+ scavenger), were used for scavenger tests.[39,40] In Figure 10a, the presence

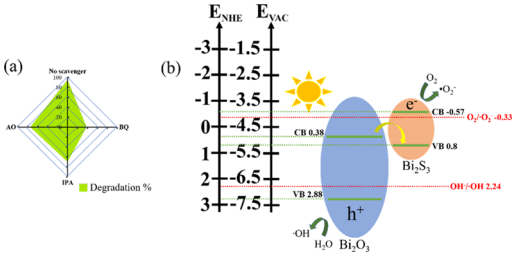

Figure 10. (a) Degradation percentage of MO solution with S1 in the presence of various scavengers. (b) Schematic diagrams of the possible photodegradation process of S1 toward MO dyes.

of BQ reduced the removal rate of MO to 46.3%, while the presence of AO and IPA had a minor effect on the degradation of MO. The possible reason is that adding BQ to the MO aqueous system will cause BQ to capture $^{\bullet}O_2^-$ and reduce the amount of active $^{\bullet}O_2^-$ radicals used in the photocatalytic reaction, deactivating the S1 photocatalyst. The scavenger test results demonstrate that the $^{\bullet}O_2^-$ is the main radical governing the photocatalytic process of S1 toward MO solution. Based on the previous results, a possible photodegradation mechanism of S1 toward MO dyes is proposed in Figure 10b. The photoinduced electrons would migrate to the CB of Bi_2O_3 from the CB of Bi_2S_3, and holes would migrate to the VB of Bi_2S_3 from the VB of Bi_2O_3 if the Bi_2O_3−Bi_2S_3 composite complies with the mechanism of type II heterojunction. However, the photoinduced holes on the VB of Bi_2S_3 are incapable of oxidizing OH^- to produce $^{\bullet}OH$ radicals because the VB edge potential of Bi_2S_3 (0.80 V vs NHE) is more negative than the potential of $OH^-/^{\bullet}OH$ (2.24 V) as presented in Figure 10b.[38] Meanwhile, the potential of $O_2/^{\bullet}O_2^-$ is −0.33 V, which is more negative than that of the CB of Bi_2O_3, so the CB electrons could not quickly reduce the O_2.[38] It should be noted that this type II mechanism could simultaneously weaken the reducing ability of photoelectrons and the oxidizing ability of photoinduced holes during the photocatalytic process according to the relative potential positions among CB of Bi_2O_3, VB of Bi_2S_3, and redox potentials. Based on the discussion above, the type II photocatalytic mechanism might not be suitable to explain the photocatalytic mechanism of S1 toward MO dyes herein. Notably, according to the analysis results of the capture experiments, the S1 photocatalyst produces superoxide radicals ($^{\bullet}O_2^-$) with strong oxidizing ability during the photocatalytic process. Moreover, $^{\bullet}OH$ and h^+ radicals also have a certain degree of activity in the photocatalytic process. These results contradict the abovementioned analysis of the type II photocatalytic mechanism. Contrarily, the scavenger test results might evidence the construction of the direct Z-scheme heterojunction in the Bi_2O_3−Bi_2S_3 composite (Figure 10b). Upon light irradiation, both Bi_2O_3 and Bi_2S_3 components are excited to generate the charge carriers in their CBs and VBs, respectively. After constructing the Z-scheme heterojunction, the photoelectrons of Bi_2O_3 in the CB position could migrate to the VB position of Bi_2S_3 through the interfacial electronic field, resulting in the effective separation of charge carriers through the Bi_2O_3/Bi_2S_3 heterojunction. Meanwhile, via this Z-scheme migration of photoinduced charge carriers, the photoelectrons and holes are gathered on a more negative CB position of Bi_2S_3 to reduce oxygen molecules into $^{\bullet}O_2^-$ radicals and a more favorable VB position of Bi_2O_3 to react with the H_2O molecules to generate the ·OH radicals, respectively. Thus, the S1 photocatalyst simultaneously possesses a substantial reduction and oxidation ability compared to the single component during the photocatalytic process toward the MO solution. The possible action trails for active species were therefore proposed below

$$Bi_2O_3(h\nu) \rightarrow Bi_2O_3(e^-) + Bi_2O_3(h^+) \quad (1)$$

$$Bi_2S_3(h\nu) \rightarrow Bi_2S_3(e^-) + Bi_2S_3(h^+) \quad (2)$$

$$e^-(\text{from } Bi_2S_3) + O_2 \rightarrow {}^{\bullet}O_2^- \quad (3)$$

$$h^+(\text{from } Bi_2O_3) + H_2O \rightarrow {}^{\bullet}OH + H^+ \quad (4)$$

$$^{\bullet}O_2^-, h^+, \text{and } {}^{\bullet}OH + MO \rightarrow CO_2 + H_2O \quad (5)$$

CONCLUSIONS

CBD-derived porous Bi_2O_3 sheets were used as a template for vulcanization to form Bi_2O_3−Bi_2S_3 composite structures. At 0.01 M vulcanization, porous and small-sized Bi_2O_3−Bi_2S_3 composite sheets were produced. At 0.1 M vulcanization, the porous Bi_2O_3−Bi_2S_3 composite sheets with a larger size will be formed. When the vulcanization concentration is increased to 1 M, the porous Bi_2O_3 sheets transform into a solid and pure Bi_2S_3 sheet structure. S1 exhibits the best light absorption, the highest photogenerated charge separation efficiency, the smallest electron transfer impedance, and the highest carrier density among various samples. Furthermore, S1 shows good durability and the best photocatalytic decomposition toward MO dyes compared to the other control samples. The improved photodegradation performance can be ascribed to constructing the direct Z-scheme heterojunction, which

https://doi.org/10.1021/acsomega.3c02153
ACS Omega 2023, 8, 26055−26064

promotes the practical separation of photoinduced charge carriers and the enhanced redox capacity. The findings herein might be of great value in developing porous oxide-sulfide composite materials for desirable photosensitive applications.

■ ASSOCIATED CONTENT

Supporting Information

The Supporting Information is available free of charge at https://pubs.acs.org/doi/10.1021/acsomega.3c02153.

TEM analysis of S2; low-magnification images; HRTEM images; SAED pattern; EDS line-scan profiles of the sample; Bi 4f XPS spectrum of S1; O 1s spectrum of S1; Bi 4f XPS spectrum of S3; absorbance spectrum of S3 (Bi_2S_3) sheets; and calculated band gap energy of S3 sheets (PDF)

■ AUTHOR INFORMATION

Corresponding Author

Yuan-Chang Liang − *Department of Optoelectronics and Materials Technology, National Taiwan Ocean University, Keelung 20224, Taiwan;* orcid.org/0000-0001-9973-1804; Email: yuanvictory@gmail.com

Authors

Yu-Hsun Chou − *Department of Optoelectronics and Materials Technology, National Taiwan Ocean University, Keelung 20224, Taiwan*

Bo-Yue Chen − *Department of Optoelectronics and Materials Technology, National Taiwan Ocean University, Keelung 20224, Taiwan*

Wei-Yang Sun − *Department of Optoelectronics and Materials Technology, National Taiwan Ocean University, Keelung 20224, Taiwan*

Complete contact information is available at: https://pubs.acs.org/10.1021/acsomega.3c02153

Notes

The authors declare no competing financial interest.

■ ACKNOWLEDGMENTS

This research was funded by the National Science and Technology Council of Taiwan, grant number MOST 111-2221-E-019-062-MY3.

■ REFERENCES

(1) Sun, B.; Feng, T. T.; Dong, J.; Li, X. L.; Liu, X. H.; Wu, J.; Ai, S. Y. Green synthesis of bismuth sulfide nanostructures with tunable morphologies and robust photoelectrochemical performance. *CrystEngComm* **2019**, *21*, 1474−1481.

(2) Yu, H.; Wang, J. L.; Wang, T. T.; Yu, H. S.; Yang, J.; Liu, G. W.; Qiao, G. J.; Yang, Q.; Cheng, X. N. Scalable colloidal synthesis of uniform Bi2S3 nanorods as sensitive materials for visible-light photodetectors. *CrystEngComm* **2017**, *19*, 727−733.

(3) Liang, Y. C.; You, S. Y.; Chen, B. Y. Crystal Design and Photoactivity of TiO_2 Nanorod Template Decorated with Nanostructured Bi_2S_3 Visible Light Sensitizer. *Int. J. Mol. Sci.* **2022**, *23*, 12024.

(4) Kim, J. H.; Ma, A. Y.; Jung, H.; Kim, H. Y.; Choe, H. R.; Kim, Y. H.; Nam, K. M. In Situ Growth of the Bi_2S_3 Nanowire Array on the Bi_2MoO_6 Film for an Improved Photoelectrochemical Performance. *ACS Omega* **2019**, *4*, 17359−17365.

(5) Fenelon, E.; Bui, D. P.; Tran, H. H.; You, S. J.; Wang, Y. F.; Cao, T. M.; Van Pham, V. Straightforward Synthesis of SnO_2/Bi_2S_3/BiOCl−$Bi_24O_{31}Cl_{10}$ Composites for Drastically Enhancing Rhodamine B Photocatalytic Degradation under Visible Light. *ACS Omega* **2020**, *5*, 20438−20449.

(6) Liu, Z. Q.; Huang, W. Y.; Zhang, Y. M.; Tong, Y. X. Facile hydrothermal synthesis of Bi_2S_3 spheres and CuS/Bi_2S_3 composites nanostructures with enhanced visible-light photocatalytic performances. *CrystEngComm* **2012**, *14*, 8261−8267.

(7) Wu, T.; Zhou, X. G.; Zhang, H.; Zhong, X. H. Bi_2S_3 nanostructures: A new photocatalyst. *Nano Res.* **2010**, *3*, 379−386.

(8) Liang, Y. C.; Chou, Y. H. Improved photoelectrode performance of chemical solution-derived Bi_2O_3 crystals via manipulation of crystal characterization. *RSC Adv.* **2020**, *10*, 45042−45058.

(9) Leng, D. H.; Wang, T. T.; Du, C. C.; Pei, X. X.; Wan, Y. X.; Wang, J. L. Synthesis of β-Bi_2O_3 nanoparticles via the oxidation of Bi nanoparticles: Size, shape and polymorph control, anisotropic thermal expansion, and visible-light photocatalytic activity. *Ceram. Int.* **2022**, *48*, 18270−18277.

(10) Cheng, H. F.; Huang, B. B.; Lu, J. B.; Wang, Z. Y.; Xu, B.; Qin, X. Y.; Zhang, X. Y.; Dai, Y. Synergistic effect of crystal and electronic structures on the visible-light-driven photocatalytic performances of Bi_2O_3 polymorphs. *Phys. Chem. Chem. Phys.* **2010**, *12*, 15468−15475.

(11) Liang, Y. C.; Chiang, K. J. Coverage Layer Phase Composition-Dependent Photoactivity of One-Dimensional TiO_2-Bi_2O_3 Composites. *Nanomaterials* **2020**, *10*, 1005.

(12) Kong, S. L.; An, Z. H.; Zhang, W. W.; An, Z. H.; Yuan, M.; Chen, D. H. Preparation of Hollow Flower-Like Microspherical β-Bi_2O_3/BiOCl Heterojunction and High Photocatalytic Property for Tetracycline Hydrochloride Degradation. *Nanomaterials* **2019**, *10*, 57.

(13) Gou, X. L.; Li, R.; Wang, G. X.; Chen, Z. X.; Wexler, D. Room-temperature solution synthesis of Bi_2O_3 nanowires for gas sensing application. *Nanotechnology* **2009**, *20*, 495501.

(14) Liang, Y. C.; Chiang, K. J. Growth temperature-dependent phase evolution and photoactivities of sputtering-deposited crystalline Bi_2O_3 thin films. *CrystEngComm* **2020**, *22*, 4215−4227.

(15) Yu, H.; Huang, J.; Zhang, H.; Zhao, Q.; Zhong, X. Nanostructure and charge transfer in Bi_2S_3-TiO_2 heterostructures. *Nanotechnology* **2014**, *25*, 215702.

(16) Liang, N.; Zai, J.; Xu, M.; Zhu, Q.; Wei, X.; Qian, X. Novel $Bi_2S_3/Bi_2O_2CO_3$ heterojunction photocatalysts with enhanced visible light responsive activity and wastewater treatment. *J. Mater. Chem. A* **2014**, *2*, 4208.

(17) Chen, X. J.; Li, N.; Zhu, R. L.; Li, S.; Yu, C. M.; Xia, W.; Xu, S.; Chen, X. Temperature-Program Assisted Synthesis of Novel Z-Scheme $CuBi_2O_4/\beta$-Bi_2O_3 Composite with Enhanced Visible Light Photocatalytic Performance. *Nanomaterials* **2018**, *8*, 579.

(18) Kim, J. H.; Lim, T. W.; Park, J. Y.; Ma, A. Y.; Jung, H.; Kim, H. Y.; Cho, S. K.; Yoon, H. N.; Nam, K. M. Understanding and improving photoelectrochemical performance of Bi_2O_3/Bi_2S_3 composite. *New J. Chem.* **2019**, *43*, 11893−11902.

(19) Chen, L.; He, J.; Yuan, Q.; Liu, Y.; Au, C. T.; Yin, S. F. Environmentally benign synthesis of branched Bi_2O_3−Bi_2S_3 photocatalysts by an etching and re-growth method. *J. Mater. Chem. A* **2015**, *3*, 1096−1102.

(20) Liang, Y. C.; Li, T. H. Controllable morphology of Bi_2S_3 nanostructures formed via hydrothermal vulcanization of Bi_2O_3 thin-film layer and their photoelectrocatalytic performances. *Nanotechnol. Rev.* **2021**, *11*, 284−297.

(21) Sirimanne, P. M.; Takahashi, K.; Sonoyama, N.; Sakata, T. Photocurrent enhancement of wide bandgap Bi_2O_3 by Bi_2S_3 over layers. *Sol. Energy Mater. Sol. Cells* **2002**, *73*, 175−187.

(22) Zhu, G.; Que, W.; Zhang, J. Synthesis and photocatalytic performance of Ag-loaded β-Bi_2O_3 microspheres under visible light irradiation. *J. Alloys Compd.* **2011**, *509*, 9479−9486.

(23) Huang, G. Z.; Zhang, J.; Jiang, F.; Zhang, Z.; Zeng, J. H.; Qi, X.; Shen, Z. J.; Wang, H. B.; Kong, Z.; Xi, J. H.; Ji, Z. G. Excellent photoelectrochemical activity of Bi_2S_3 nanorod/TiO_2 nanoplate composites with dominant {001} facets. *J. Solid State Chem.* **2020**, *281*, 121041.

(24) Ma, Y. Y.; Jiang, X.; Sun, R. K.; Yang, J. L.; Jiang, X. L.; Liu, Z. Q.; Xie, M. Z.; Xie, E. Q.; Han, W. H. Z-scheme $Bi_2O_{2.33}/Bi_2S_3$

heterojunction nanostructures for photocatalytic overall water splitting. *Chem. Eng. J.* **2020**, *382*, 123020.
(25) Ghosh, K.; Srivastava, S. K. Superior supercapacitor performance of Bi_2S_3 nanorod/reduced graphene oxide composites. *Dalton Trans.* **2020**, *49*, 16993−17004.
(26) McCrory, C. C. L.; Jung, S.; Peters, J. C.; Jaramillo, T. F. Benchmarking Heterogeneous Electrocatalysts for the Oxygen Evolution Reaction. *J. Am. Chem. Soc.* **2013**, *135*, 16977−16987.
(27) Gao, Y.; Zhang, N.; Wang, C.; Zhao, F.; Yu, Y. Construction of Fe2O3@CuO Heterojunction Nanotubes for Enhanced Oxygen Evolution Reaction. *ACS Appl. Energy Mater.* **2020**, *3*, 666−674.
(28) Tang, Y.; Fang, X.; Zhang, X.; Fernandes, G.; Yan, Y.; Yan, D.; Xiang, X.; He, J. Space-confined earth-abundant bifunctional electrocatalyst for high-efficiency water splitting. *ACS Appl. Mater. Interfaces* **2017**, *9*, 36762−36771.
(29) Mahala, C.; Sharma, M. D.; Basu, M. ZnO Nanosheets Decorated with Graphite-Like Carbon Nitride Quantum Dots as Photoanodes in Photoelectrochemical Water Splitting. *ACS Appl. Nano Mater.* **2020**, *3*, 1999−2007.
(30) Yan, Y. X.; Yang, H.; Yi, Z.; Xian, T.; Wang, X. X. Direct Z-scheme $CaTiO_3$@BiOBr composite photocatalysts with enhanced photodegradation of dyes. *Environ. Sci. Pollut. Res.* **2019**, *26*, 29020−29031.
(31) Guan, Z. C.; Wang, H. P.; Wang, X.; Hu, J.; Du, R. G. Fabrication of heterostructured β-Bi_2O_3-TiO_2 nanotube array composite film for photoelectrochemical cathodic protection applications. *Corros. Sci.* **2018**, *136*, 60−69.
(32) Atta, N. F.; Ibrahim, A. H.; Galal, A. Nickel oxide nanoparticles/ionic liquid crystal modified carbon composite electrode for determination of neurotransmitters and paracetamol. *New J. Chem.* **2016**, *40*, 662−673.
(33) Liu, Q.; Lu, H.; Shi, Z.; Wu, F.; Guo, J.; Deng, K.; Li, L. 2D $ZnIn_2S_4$ Nanosheet/1D TiO_2 Nanorod Heterostructure Arrays for Improved Photoelectrochemical Water Splitting. *ACS Appl. Mater. Interfaces* **2014**, *6*, 17200−17207.
(34) Li, X.; Yu, J. G.; Low, J. X.; Fang, Y. P.; Xiao, J.; Chen, X. B. Engineering heterogeneous semiconductors for solar water splitting. *J. Mater. Chem. A* **2015**, *3*, 2485−2534.
(35) Guo, R. N.; Zhu, G. X.; Gao, Y. J.; Li, B.; Gou, J. F.; Cheng, X. W. Synthesis of 3D Bi_2S_3/TiO_2 NTAs photocatalytic system and its high visible light driven photocatalytic performance for organic compound degradation. *Sep. Purif. Technol.* **2019**, *226*, 315−322.
(36) Bu, Y. Y.; Chen, Z. Y. Effect of hydrogen treatment on the photoelectrochemical properties of quantum dots sensitized ZnO nanorod array. *J. Power Sources* **2014**, *272*, 647−653.
(37) Liang, Y. C.; Chiang, K. J. Design and tuning functionality of rod-like titanium dioxide−nickel oxide composites via a combinational methodology. *Nanotechnology* **2020**, *31*, 195709.
(38) Zhu, L. Y.; Li, H.; Xia, P. F.; Liu, Z. R.; Xiong, D. H. Hierarchical ZnO Decorated with CeO_2 Nanoparticles as the Direct Z-Scheme Heterojunction for Enhanced Photocatalytic Activity. *ACS Appl. Mater. Interfaces* **2018**, *10*, 39679−39687.
(39) Xu, Y. S.; Zhang, W. D. Anion exchange strategy for construction of sesame-biscuit-like $Bi_2O_2CO_3$/Bi_2MoO_6 nanocomposites with enhanced photocatalytic activity. *Appl. Catal., B* **2013**, *140−141*, 306−316.
(40) Xiao, X.; Hu, R. P.; Tu, S. H.; Zheng, C. X.; Zhong, H.; Zuo, X. X.; Nan, J. M. One-pot synthesis of micro/nano structured β-Bi_2O_3 with tunable morphology for highly efficient photocatalytic degradation of methylparaben under visible-light irradiation. *RSC Adv.* **2015**, *5*, 38373−38381.

https://doi.org/10.1021/acsomega.3c02153
ACS Omega 2023, 8, 26055−26064